

August 26, 2022

# Vibrationally resolved electronic spectra including vibrational pre-excitation: Theory and application to VIPER spectroscopy

Jan von Cosel,<sup>1</sup> Javier Cerezo,<sup>2</sup> Daniela Kern-Michler,<sup>3</sup>  
 Carsten Neumann,<sup>3</sup> Luuk J. G. W van Wilderen,<sup>3</sup> Jens Bredenbeck,<sup>3</sup>  
 Fabrizio Santoro,<sup>4,a)</sup> and Irene Burghardt<sup>1,a)</sup>

<sup>1</sup>*Institute of Physical and Theoretical Chemistry,*

*Goethe University Frankfurt, Max-von-Laue-Str. 7, 60438 Frankfurt, Germany*

<sup>2</sup>*Departamento de Química Física, Universidad de Murcia, E-30071 Murcia, Spain*

<sup>3</sup>*Institute of Biophysics, Goethe University Frankfurt,*

*Max-von-Laue-Str. 1, 60438 Frankfurt, Germany*

<sup>4</sup>*Consiglio Nazionale delle Ricerche – CNR, Istituto di Chimica dei Composti Organo  
 Metallici (ICCOM-CNR), UOS di Pisa, Via G. Moruzzi 1, I-56124 Pisa, Italy*

<sup>a)</sup>Authors to whom correspondence should be addressed. Electronic mail:  
 fabrizio.santoro@pi.iccom.cnr.it, burghardt@theochem.uni-frankfurt.de

## Abstract

Vibrationally resolved electronic absorption spectra including the effect of vibrational pre-excitation are computed in order to interpret and predict vibronic transitions that are probed in the Vibrationally Promoted Electronic Resonance (VIPER) experiment [L. J. G. W. van Wilderen et al., *Angew. Chem. Int. Ed.* **53**, 2667 (2014)]. To this end, we employ time-independent and time-dependent methods based on the evaluation of Franck-Condon overlap integrals and Fourier transformation of time-domain wavepacket autocorrelation functions, respectively. The time-independent approach uses a generalized version of the *FCclasses* method [F. Santoro et al., *J. Chem. Phys.* **126**, 084509 (2007)]. In the time-dependent approach, autocorrelation functions are obtained by wavepacket propagation and by evaluation of analytic expressions, within the harmonic approximation including

Duschinsky rotation effects. For several medium-sized polyatomic systems, it is shown that selective pre-excitation of particular vibrational modes leads to a redshift of the low-frequency edge of the electronic absorption spectrum, which is a prerequisite for the VIPER experiment. This effect is typically most pronounced upon excitation of ring distortion modes within an aromatic  $\pi$ -system. Theoretical predictions as to which modes show the strongest VIPER effect are found to be in excellent agreement with experiment.

## I. Introduction

Combined electronic-vibrational spectroscopies pave the way for new strategies of probing and controlling molecular systems.<sup>1</sup> This is exemplified by the recently introduced Vibrationally Promoted Electronic Resonance (VIPER) experiment<sup>1,2</sup> where selective infrared (IR) excitation in the electronic ground state precedes visible (VIS) excitation, as sketched in Fig. 1. The VIPER pulse sequence was originally designed in the context of chemical exchange,<sup>2</sup> but also lends itself to inducing selective cleavage of photolabile protecting groups through the use of selective IR excitation and isotope substitution. For example, substitution of  $^{12}\text{C}$  by  $^{13}\text{C}$  leaves the electronic absorption spectrum virtually unchanged while the frequencies of vibrational modes can be altered significantly. Different isotopomers can therefore be distinguished by their IR spectra and selectively excited using narrow-band IR pulses.<sup>3</sup>

In the present work, we compute vibrationally resolved electronic absorption spectra including the effect of vibrational pre-excitation, in order to predict VIPER-active modes for several polyatomic chromophores, some of which have already been experimentally investigated. Notably, the laser dye Coumarin 6 is studied, which has served for demonstration of VIPER’s capability to measure exchange beyond the vibrational  $T_1$  lifetime.<sup>1</sup> Furthermore, [7-(diethylamino)coumarin-4-yl]methyl-azide (DEACM- $\text{N}_3$ ) and *para*-Hydroxyphenacyl thiocyanate (*p*HP-SCN) are investigated, which are model systems for photo-cleavable caging groups,<sup>4</sup> with the azide and thiocyanate groups representing the relevant leaving groups. Furthermore, we aim to establish a general understanding of which properties favor large spectral shifts that permit effective VIPER excitation. While we do not simulate the complete pump-probe type pulse sequence shown in Fig. 1, our analysis of the vibronic spectra resulting from the combined IR-pump/VIS-pump steps, is suitable for the analysis and prediction of the relevant VIPER shifts.

We apply both time-independent (TI) and time-dependent (TD) methods in conjunction with a vibronic model Hamiltonian that is parametrized in the full normal-mode space, based upon ground-state and excited-state electronic structure calculations. Besides displacements of the equilibrium geometry, the Hamiltonian accurately represents Duschinsky rotation effects.

The TI approach uses a generalized version of the *FCclasses* method developed by

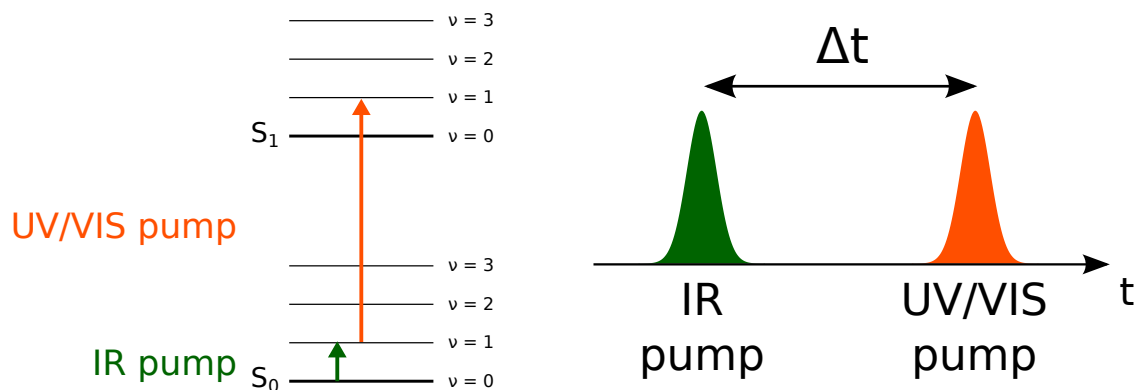


Figure 1: Left: The mixed IR/VIS VIPER excitation scheme. Right: Time-domain VIPER excitation sequence.

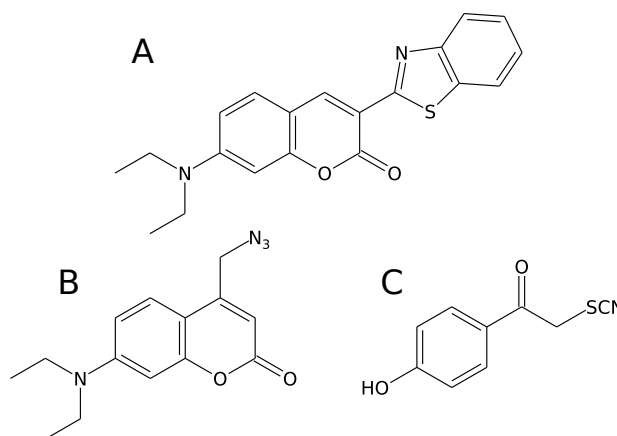


Figure 2: Structure of Coumarin 6 (**A**), [7-(diethylamino)coumarin-4-yl]methyl-azide (**B**) and *para*-hydroxyphenacyl thiocyanate (**C**).

one of us,<sup>5,6,7</sup> where a pre-screening technique is adopted to select the relevant Franck-Condon (FC) overlap integrals and obtain fully converged spectra even for high-dimensional molecular systems. In the present context, this approach was specifically adapted such as to include selective vibrational pre-excitation.

In a complementary fashion, TD methods are employed in order to compute wavepacket autocorrelation functions, whose Fourier transforms yield the vibronic absorption spectrum. Within the harmonic approximation and including vibrational pre-excitation, autocorrelation functions are either computed analytically or else using the Multi-Layer Multiconfiguration Time-Dependent Hartree (ML-MCTDH) method,<sup>8,9</sup> a recently developed variant of the MCTDH method.<sup>10,11,12</sup> In the present context, all methods are expected to give the same results for zero-temperature calculations including pre-excitation, but the

efficiency of these methods differs as a function of dimensionality and temperature effects.

The remainder of the manuscript is organized as follows. Sec. II details the TI and TD approaches employed in this study and Sec. III introduces an analysis in terms of spectral moments. Sec. IV summarizes the computational procedure, and Sec. V presents results obtained for three representative chromophores, together with experimental results for two of these systems. Sec. VI gives a discussion of the results and Sec. VII concludes. Finally, several Appendixes add information complementary to the main text.

## II. Methods for the computation of vibrationally resolved electronic spectra from a vibrationally pre-excited state

Conventionally, the computation of vibrationally resolved electronic spectra proceeds from a thermally averaged ensemble of excited vibrational states, populated according to a Boltzmann distribution.<sup>6</sup> In contrast, the present study is concerned with vibronic excitation from a non-equilibrium state where a single vibrational normal mode is placed into its first excited state by vibrational pre-excitation, while all other normal modes remain in their respective ground state. For the most part, our study will be restricted to a zero-temperature setting and we will focus on pre-excitations along high-frequency modes for which thermal excitation is negligible.

Vibrational states are defined in terms of the number of quanta in each vibrational normal mode:  $|\mathbf{w}\rangle = |w_1\rangle \otimes |w_2\rangle \otimes \cdots \otimes |w_{N_{vib}}\rangle$ . A vibrational state with pre-excitation of the  $k$ th mode is denoted by  $|\mathbf{w}'_k\rangle = |0_1\rangle \otimes |0_2\rangle \cdots |1_k\rangle \cdots |0_{N_{vib}-1}\rangle \otimes |0_{N_{vib}}\rangle = |\mathbf{0} + 1_k\rangle$ . Combined vibrational-electronic (i.e., vibronic) states are denoted  $|\psi\rangle = |\mathbf{w}\rangle \otimes |n\rangle$  where the electronic space  $\{|n\rangle\}$  is restricted to the electronic ground state ( $|g\rangle$ ) and an excited state ( $|e\rangle$ ) in the following discussion.

We are going to work in a normal-mode representation throughout, taking into account that the normal modes of the initial state  $\mathbf{Q}'$  and the final state  $\mathbf{Q}$  are different. Neglecting the effects of rotation, these sets of modes can be related by a linear transformation as described by Duschinsky<sup>13</sup>:

$$\mathbf{Q}' = \mathbf{J}\mathbf{Q} + \mathbf{K} \quad (1)$$

where the transformation matrix  $\mathbf{J}$  and the displacement vector  $\mathbf{K}$  are defined by

$$\mathbf{J} = \mathbf{L}'^{-1}\mathbf{L} \quad \text{and} \quad \mathbf{K} = \mathbf{L}'^{-1}(\mathbf{q}^{\text{eq}} - \mathbf{q}'^{\text{eq}}) \quad (2)$$

with  $\mathbf{L}$  the normal-mode matrix relating the normal modes  $\mathbf{Q}$  to mass-weighted Cartesian coordinates  $\mathbf{q} = (q_1, q_2, \dots, q_{3N})$ ,

$$\mathbf{Q} = \mathbf{L}^{-1}(\mathbf{q} - \mathbf{q}^{\text{eq}}) \quad (3)$$

In Eq. (2) and Eq. (3), the equilibrium structures of the initial and final state are termed  $\mathbf{q}'^{\text{eq}}$  and  $\mathbf{q}^{\text{eq}}$ .

In the following, the time-independent and time-dependent approaches will be detailed.

## A. Time-independent methods

In the time-independent picture, the complete spectrum can be thought of as a weighted superposition of vibronic (combined electronic and vibrational) transitions. This method is also known as the sum-over-states method. The absorption spectrum from the ground state  $|g\rangle$  to an excited state  $|e\rangle$  can then be described as follows,<sup>5,17</sup>

$$\sigma_{\text{abs}}(\omega) = \frac{4\pi^2\omega}{3c} \sum_{\mathbf{w}} |\mu_{\mathbf{w}',\mathbf{w}}|^2 \delta(E_{\mathbf{w}'} - E_{\mathbf{w}} + \hbar\omega) \quad (4)$$

where  $E_{\mathbf{w}'}$  and  $E_{\mathbf{w}}$  are the energies of the initial and final vibronic states, respectively and  $\mu_{\mathbf{w}',\mathbf{w}} = \langle \mathbf{w}' | \langle e | \hat{\mu} | g \rangle | \mathbf{w} \rangle = \langle \mathbf{w}' | \mu_{eg}(\mathbf{Q}) | \mathbf{w} \rangle$  is the transition dipole moment between the states.

Here, we will work within the Condon approximation, where the electronic transition dipole moment is assumed to be coordinate-independent,  $\mu_{eg} = \mu_0 = \text{const.}$  In this case  $\mu_{\mathbf{w}',\mathbf{w}} = \mu_0 \langle \mathbf{w}' | \mathbf{w} \rangle$  where  $\langle \mathbf{w}' | \mathbf{w} \rangle$  is the multidimensional FC overlap integral between the initial and final vibrational states.

As a result, the time-independent framework for the computation of Eq. (4) focuses upon the calculation of the FC overlap integrals  $\langle \mathbf{w}' | \mathbf{w} \rangle$  between the initial and final vibrational states. In practice, it turns out that even in medium-sized molecules, the number of possible final vibrational states  $|\mathbf{w}\rangle$  is so large that the calculation of all FC integrals is not feasible and a suitable subset must be selected. Here, we follow a scheme proposed by one of us<sup>5</sup> where the vibrational states are partitioned into so-called classes  $C_n$  where  $n$  is the number of simultaneously excited normal modes in the final state  $|\mathbf{w}\rangle$  (*FCclasses* method<sup>14</sup>).

Naturally, the number of states in each class grows rapidly with increasing  $n$ . For a spectrum at  $T = 0\text{ K}$ , all integrals, up to sufficiently high maximum quantum numbers, are computed for the first two classes  $C_1$  and  $C_2$ . Using these data, an iterative procedure determines the best set of quantum numbers for class  $C_n$  (up to  $C_7$ ) under the constraint that the total number of integrals to be computed for each class does not exceed a pre-set maximum number  $N_{\text{max}}$ . By increasing  $N_{\text{max}}$  the method can be converged to arbitrary accuracy.

Spectra from initial states that are vibrationally excited ( $|\mathbf{w}'_k\rangle$ ) are computed adopting a modified strategy developed for thermally excited states.<sup>6</sup> In these cases, both the  $C_1$  and

$C_2$  transitions from the ground state ( $|\mathbf{0}\rangle$ ) and the excited state ( $|\mathbf{w}'_k\rangle$ ) are computed and used to select the relevant transitions of higher classes. As one would intuitively expect, excitations of the final-state modes that are most similar to those excited in the initial state are particularly important to reach reasonable convergence of the spectra. Therefore the subset of final-state modes that project upon the initial-state excited vibrational modes is determined and, for high classes  $C_n$  ( $n > n_{\max}$ ), final vibrational states where these modes are not excited are neglected. Usually  $n_{\max} = 5$  provides a good compromise between accuracy and computational cost.

## B. Time-dependent methods

The time-independent expression for the spectrum Eq. (4) can be reformulated in a time-dependent framework as the Fourier transform of an autocorrelation function:<sup>15,17</sup>

$$\sigma_{\text{abs}}(\omega) = \frac{2\pi\omega}{3c} \int \chi(t, T) e^{i(\omega - E_{\text{ad}}/\hbar)t} dt \quad (5)$$

where  $E_{\text{ad}}$  is the zeroth-order (adiabatic) energy difference between the two states' minima. In general, the autocorrelation function  $\chi(t, T)$  can be expressed as follows<sup>15,16,17</sup>:

$$\chi(t, T) = \text{Tr} \left[ \hat{\mu}_{eg} e^{-i\hat{H}_e t/\hbar} \hat{\mu}_{eg} e^{i\hat{H}_g t/\hbar} \hat{\rho}_g(0) \right] \quad (6)$$

where  $\text{Tr}$  denotes the trace operation, and  $\hat{\rho}_g(0)$  is the combined vibrational and electronic density operator referring to the initial state ( $g$ ), i.e.,  $\hat{\rho}_g(0) = \hat{\rho}_g^{\text{vib}}(0) \otimes |g\rangle\langle g|$ . The dipole operator is again taken to be coordinate independent,  $\hat{\mu}_{eg} = \mu_0(|e\rangle\langle g| + \text{h.c.})$ , and  $\hat{H}_g$  and  $\hat{H}_e$  are the Hamiltonians of the ground state and the excited state, respectively.

General expressions for the above autocorrelation function starting from a thermally populated initial state have been discussed elsewhere,<sup>15,16,18</sup> and the autocorrelation function for a 0 K state has been derived in Ref. [18]. Here, we focus specifically upon the case of an initial vibrationally pre-excited state at 0 K,

$$\hat{\rho}_g(0) = |\mathbf{0} + 1_k\rangle\langle \mathbf{0} + 1_k| \quad (7)$$

leading to the following form of the autocorrelation function,

$$\chi(t, T=0) \equiv \chi_k(t) = \mu_0^2 e^{i(E_0/\hbar + \omega_{gk})t} \left\langle \mathbf{0} + 1_k \left| e^{-i\hat{H}_e t} \right| \mathbf{0} + 1_k \right\rangle \quad (8)$$

where  $E_0$  is the vibrational zero-point energy of the initial state and  $\omega_{gk}$  is the angular frequency of the pre-excited mode.

In the following, two approaches of obtaining the correlation function are introduced, i.e., by evaluation of analytical expressions and by numerical wavepacket propagation, respectively. Within the harmonic approximation, both approaches give the same result. In situations where anharmonicity or non-adiabatic couplings play an important role, it is mandatory, though, to switch to more general technique of wavepacket propagation, making no assumptions about the shape of the potential energy surfaces (PESs).

## 1. Analytical expression for the autocorrelation function

To obtain an analytical expression for  $\chi_k(t)$  of Eq. (8), we employ the normal-mode representation, in line with the treatment of Refs. [16,18,19]. Since the initial state normal modes  $\mathbf{Q}_g$  form a complete basis set, the coordinate representation of  $\chi_k(t)$  can be written as follows by inserting the identity twice,

$$\chi_k(t) = \mu_0^2 e^{i(E_0/\hbar + \omega_{gk})t} \int d\bar{\mathbf{Q}}_g \int d\mathbf{Q}_g \langle \mathbf{0} + 1_k | \mathbf{Q}_g \rangle \langle \mathbf{Q}_g | e^{-i\hat{H}_e t} | \bar{\mathbf{Q}}_g \rangle \langle \bar{\mathbf{Q}}_g | \mathbf{0} + 1_k \rangle. \quad (9)$$

The coordinate representation of the vibrationally pre-excited initial state is given as follows,

$$\langle \mathbf{Q}_g | \mathbf{0} + 1_k \rangle = Q_k \sqrt{2\Gamma_{gk}} \langle \mathbf{Q}_g | \mathbf{0} \rangle \quad (10)$$

with the harmonic oscillator ground state

$$\langle \mathbf{Q}_g | \mathbf{0} \rangle = \frac{\det(\mathbf{\Gamma}_g)^{1/4}}{\pi^{N/4}} \exp \left[ -\frac{\mathbf{Q}_g^T \mathbf{\Gamma}_g \mathbf{Q}_g}{2} \right] \quad (11)$$

where  $\mathbf{\Gamma}_g$  is a diagonal matrix containing the reduced frequencies of the initial state ( $g$ ) normal modes  $(\mathbf{\Gamma}_g)_{kk} = \Gamma_{gk} = \omega_{gk}/\hbar$ . From eqs. (10)-(11), we note that  $\langle \mathbf{Q}_g | \mathbf{0} + 1_k \rangle = \langle \mathbf{0} + 1_k | \mathbf{Q}_g \rangle$ . Inserting the latter expression into Eq. (9) results in

$$\chi_k(t) = 2\mu_0^2 \Gamma_{gk} e^{i(E_0/\hbar + \omega_{gk})t} \frac{\det(\mathbf{\Gamma}_g)^{1/2}}{\pi^{N/2}} \int d\bar{\mathbf{Q}}_g \int d\mathbf{Q}_g Q_{gk} \bar{Q}_{gk} \exp \left[ -\frac{\mathbf{Q}_g^T \mathbf{\Gamma}_g \mathbf{Q}_g}{2} \right] \langle \mathbf{Q}_g | e^{-i\hat{H}_e t} | \bar{\mathbf{Q}}_g \rangle \exp \left[ -\frac{\bar{\mathbf{Q}}_g^T \mathbf{\Gamma}_g \bar{\mathbf{Q}}_g}{2} \right]. \quad (12)$$

In order to represent the matrix element of the final state propagator,  $\langle \mathbf{Q}_g | e^{-i\hat{H}_e t} | \bar{\mathbf{Q}}_g \rangle$  in terms of the final state normal modes, we now introduce two complete sets of final state coordinates  $\mathbf{Q}_e$ :

$$\chi_k(t) = 2\mu_0^2 \Gamma_{gk} e^{i(E_0/\hbar + \omega_{gk})t} \frac{\det(\mathbf{\Gamma}_g)^{1/2}}{\pi^{N/2}} \int d\bar{\mathbf{Q}}_g \int d\mathbf{Q}_g \int d\bar{\mathbf{Q}}_e \int d\mathbf{Q}_e Q_{gk} \bar{Q}_{gk} \exp \left[ -\frac{\mathbf{Q}_g^T \mathbf{\Gamma}_g \mathbf{Q}_g}{2} \right] \langle \mathbf{Q}_g | \mathbf{Q}_e \rangle \langle \mathbf{Q}_e | e^{-i\hat{H}_e t} | \bar{\mathbf{Q}}_e \rangle \langle \bar{\mathbf{Q}}_e | \bar{\mathbf{Q}}_g \rangle \exp \left[ -\frac{\bar{\mathbf{Q}}_g^T \mathbf{\Gamma}_g \bar{\mathbf{Q}}_g}{2} \right]. \quad (13)$$

We can now use Feynman's path integral expression to evaluate the matrix element of the propagator

$$\langle \mathbf{Q}_e | e^{-i\hat{H}_e t} | \bar{\mathbf{Q}}_e \rangle = \sqrt{\frac{\det(\mathbf{a}_e(t))}{(2\pi i \hbar)^N}} \exp \left\{ \frac{i}{\hbar} \left[ \frac{1}{2} \mathbf{Q}_e^T \mathbf{b}_e(t) \mathbf{Q}_e + \frac{1}{2} \bar{\mathbf{Q}}_e^T \mathbf{b}_e(t) \bar{\mathbf{Q}}_e - \mathbf{Q}_e^T \mathbf{a}_e(t) \bar{\mathbf{Q}}_e \right] \right\}, \quad (14)$$

where  $\mathbf{a}_e(t)$  and  $\mathbf{b}_e(t)$  are diagonal matrices with

$$(\mathbf{a}_e)_{kk}(t) \equiv a_{ek}(t) = \frac{\Gamma_{ek}}{\sin(\hbar\Gamma_{ek}t)} \quad \text{and} \quad (\mathbf{b}_e)_{kk}(t) \equiv b_{ek}(t) = \frac{\Gamma_{ek}}{\tan(\hbar\Gamma_{ek}t)}. \quad (15)$$

Since  $\mathbf{Q}_g$  and  $\mathbf{Q}_e$  are orthonormal, the overlap is given as  $\langle \mathbf{Q}_g | \mathbf{Q}_e \rangle = \delta(\mathbf{Q}_g - \mathbf{J}\mathbf{Q}_e - \mathbf{K})$ . Inserting these relations into Eq. (13) results in the Gaussian integral

$$\begin{aligned} \chi_k(t) = 2\mu_0^2 \Gamma_{gk} e^{i(E_0/\hbar + \omega_{gk})t} & \sqrt{\frac{\det(\mathbf{\Gamma}_g) \det(\mathbf{a}_e(t))}{\pi^N (2\pi i \hbar)^N}} \exp \left[ -\mathbf{K}^T \mathbf{\Gamma}_g \mathbf{K} \right] \int d\bar{\mathbf{Q}}_e \int d\mathbf{Q}_e \\ & \left( K_k^2 + K_k \sum_l J_{kl} (Q_{el} + \bar{Q}_{el}) + \sum_l \sum_m J_{kl} J_{km} Q_{el} \bar{Q}_{em} \right) \\ & \exp \left\{ \frac{i}{\hbar} \left[ i\hbar \mathbf{K}^T \mathbf{\Gamma}_g \mathbf{J} (\mathbf{Q}_e + \bar{\mathbf{Q}}_e) + \frac{1}{2} \mathbf{Q}_e^T \mathbf{B}(t) \mathbf{Q}_e + \frac{1}{2} \bar{\mathbf{Q}}_e^T \mathbf{B}(t) \bar{\mathbf{Q}}_e - \mathbf{Q}_e^T \mathbf{a}_e(t) \bar{\mathbf{Q}}_e \right] \right\} \end{aligned} \quad (16)$$

where we introduced the matrix

$$\mathbf{B}(t) = i\hbar \mathbf{J}^T \mathbf{\Gamma}_g \mathbf{J} + \mathbf{b}_e(t) \quad (17)$$

As detailed in Appendix A, this expression can be integrated analytically and is further recast as follows in a compact and transparent form,

$$\chi_k(t) = 2\Gamma_{gk} e^{i\hbar\Gamma_{gk}t} \chi_{FC}^0(t) \left( K_k^2 + 2 \sum_i K_k J_{ki} \tilde{\mathbf{D}}_i(t) + \sum_{ij} J_{ki} J_{kj} \tilde{\mathbf{A}}_{ij}(t) \right) \quad (18)$$

where  $\chi_{FC}^0(t)$  is the autocorrelation function at 0 K<sup>18</sup> in the absence of initial vibrational excitation,

$$\chi_{FC}^0(t) = \mu_0^2 \sqrt{\frac{\det(\mathbf{a}'_g(t) \mathbf{a}_e(t))}{(i\hbar)^{2N} \det(\mathbf{C}\mathbf{D})}} \exp \left[ -\mathbf{K}^T \mathbf{\Gamma}_g \mathbf{K} + \boldsymbol{\lambda}^T \mathbf{D}^{-1} \boldsymbol{\lambda} \right], \quad (19)$$

with  $\boldsymbol{\lambda}^T = \mathbf{K}^T \mathbf{\Gamma}_g \mathbf{J}$ . Further, the following auxiliary quantities were introduced,

$$\begin{aligned} \tilde{\mathbf{D}}(t) &= -\mathbf{D}^{-1}(t) \mathbf{J}^T \mathbf{\Gamma}_g \mathbf{K} \\ \tilde{\mathbf{A}}(t) &= \tilde{\mathbf{D}}(t) \tilde{\mathbf{D}}^T(t) + \frac{1}{2} \left( \mathbf{D}^{-1}(t) - \mathbf{C}^{-1}(t) \right) \end{aligned} \quad (20)$$

and, in turn,

$$\begin{aligned} \mathbf{C}(t) &= -\frac{i}{\hbar} (\mathbf{B}(t) + \mathbf{a}_e(t)) \\ \mathbf{D}(t) &= -\frac{i}{\hbar} (\mathbf{B}(t) - \mathbf{a}_e(t)) \end{aligned} \quad (21)$$

where  $\mathbf{B}(t) = i\hbar \mathbf{J}^T \mathbf{\Gamma}_g \mathbf{J} + \mathbf{b}_e(t)$ . The above expressions for  $\tilde{\mathbf{D}}$  and  $\tilde{\mathbf{A}}$  and the overall expression for the correlation function are very similar to expressions that were previously obtained to describe Herzberg-Teller transitions, where the transition dipole depends linearly on the coordinates.<sup>16,18,19</sup>



## 2. Autocorrelation function by wavepacket propagation

The autocorrelation function of Eq. (8) can be obtained alternatively by propagating a wavepacket corresponding to the initial vibrational state  $|\mathbf{0} + 1_k\rangle$  evolving on the excited-state PES,

$$|\psi_e(0)\rangle = |\mathbf{0} + 1_k\rangle \otimes |e\rangle \quad (22)$$

such that<sup>17</sup>

$$\begin{aligned} \chi_k(t) &= \mu_0^2 e^{i(E_0/\hbar + \omega_{gk})t} \langle \psi_e(0) | e^{-i\hat{H}_e t} | \psi_e(0) \rangle \\ &= \mu_0^2 e^{i(E_0/\hbar + \omega_{gk})t} \langle \psi_e(0) | \psi_e(t) \rangle \end{aligned} \quad (23)$$

In this approach, it is convenient to work in the normal-mode representation of the electronic ground state ( $g$ ), where the initial wavefunction is separable with respect to the normal-mode eigenfunctions, one of which corresponds to a vibrationally excited state,

$$|\psi_e(\mathbf{Q}_g, 0)\rangle = \left( \varphi_{k1}(Q_{gk}) \prod_{n \neq k} \varphi_{n0}(Q_{gn}) \right) \otimes |e\rangle \quad (24)$$

Propagation necessitates a representation of the excited-state PES in terms of ground-state normal modes, which is obtained as follows, using the transformation Eq. (1). Given that the excited-state PES is diagonal in terms of its normal modes:

$$V_e(\mathbf{Q}) = \frac{1}{2} \mathbf{Q}^T \mathbf{F} \mathbf{Q} + E_{\text{ad}} \quad (25)$$

where  $\mathbf{F}$  is the diagonal matrix of the final state normal mode's force constants, we can invert Eq. (1) to yield

$$\mathbf{Q} = \tilde{\mathbf{J}} \mathbf{Q}' + \tilde{\mathbf{K}} \quad \text{with} \quad \tilde{\mathbf{J}} = \mathbf{J}^T \quad \text{and} \quad \tilde{\mathbf{K}} = -\mathbf{J}^T \mathbf{K}. \quad (26)$$

Inserting this expression for  $\mathbf{Q}$  into Eq. (25), we obtain

$$V_e(\mathbf{Q}') = \frac{1}{2} (\tilde{\mathbf{J}} \mathbf{Q}' + \tilde{\mathbf{K}})^T \mathbf{F} (\tilde{\mathbf{J}} \mathbf{Q}' + \tilde{\mathbf{K}}) + E_{\text{ad}} \quad (27)$$

$$= \frac{1}{2} \mathbf{Q}'^T \tilde{\mathbf{J}}^T \mathbf{F} \tilde{\mathbf{J}} \mathbf{Q}' + \tilde{\mathbf{K}}^T \mathbf{F} \tilde{\mathbf{J}} \mathbf{Q}' + \frac{1}{2} \tilde{\mathbf{K}}^T \mathbf{F} \tilde{\mathbf{K}} + E_{\text{ad}} \quad (28)$$

and going back to the original  $\mathbf{J}$  and  $\mathbf{K}$ , the final expression for the PES reads

$$V_e(\mathbf{Q}') = \frac{1}{2} \mathbf{Q}'^T \mathbf{J} \mathbf{F} \mathbf{J}^T \mathbf{Q}' - \mathbf{K}^T \mathbf{J} \mathbf{F} \mathbf{J}^T \mathbf{Q}' + \frac{1}{2} \mathbf{K}^T \mathbf{J} \mathbf{F} \mathbf{J}^T \mathbf{K} + E_{\text{ad}} \quad (29)$$

This expression for the excited-state PES has been employed in conjunction with the ML-MCTDH wavepacket propagation method, as further detailed below.

### III. Analysis of computed spectra

In order to quantitatively characterize the influence of vibrational pre-excitation on the electronic absorption spectrum, it is useful to analyze its influence on the first and second spectral moments. The first moment is equivalent to the expectation value or the center of gravity of the spectrum, whereas the second moment corresponds to the width. In general, the  $N$ th moment of a continuous distribution function is given by

$$\mathcal{M}^{(N)} = \int_{-\infty}^{\infty} x^N f(x) dx. \quad (30)$$

For the spectrum computed at the FC level within the harmonic approximation, the first and second moments can be calculated analytically.<sup>20</sup> The first moment of a spectrum starting from the vibrational ground state  $|0\rangle$  state is given by

$$\mathcal{M}_0^{(1)} = E_{\text{ad}} + \frac{1}{2} \mathbf{K}^T \widetilde{\mathbf{F}} \mathbf{K} + \frac{1}{4} \sum_i \frac{\widetilde{F}_{ii} - \Omega_i^2}{\Omega_i}, \quad (31)$$

where  $\Omega_i$  is the frequency of the  $i$ th ground state normal mode and  $\widetilde{\mathbf{F}} = \mathbf{J} \mathbf{F} \mathbf{J}^T$  is the matrix of the excited state force constants projected onto the ground state normal modes (cf. Eq. (29)). The second moment reads (see Ref. [20] for a more general expression including temperature effects)

$$\begin{aligned} \mathcal{M}_0^{(2)} = E_v^2 + \frac{E_v}{2} \sum_i \frac{\widetilde{F}_{ii} - \Omega_i^2}{\Omega_i} + \frac{1}{8} \sum_i \sum_{j>i} \frac{(\widetilde{F}_{ii} - \Omega_i^2)(\widetilde{F}_{jj} - \Omega_j^2)}{\Omega_i \Omega_j} + \frac{1}{2} \sum_i \frac{g_i^2}{\Omega_i} \\ + \frac{3}{8} \sum_i \frac{(\widetilde{F}_{ii} - \Omega_i^2)^2}{\Omega_i^2} + \frac{1}{2} \sum_i \sum_{j>i} \frac{\widetilde{F}_{ij}^2}{\Omega_i \Omega_j} \end{aligned} \quad (32)$$

where  $E_v$  is the vertical transition energy at the ground state minimum, corresponding to the first two terms in Eq. (31) and  $\mathbf{g} = -\mathbf{K}^T \widetilde{\mathbf{F}}$  is the gradient on the PES of the excited state along the ground state normal modes. If we start from a pre-excited state  $|0 + 1_k\rangle$ , the first moment is given by

$$\mathcal{M}_k^{(1)} = \mathcal{M}_0^{(1)} + \frac{1}{2} \frac{\widetilde{F}_{kk} - \Omega_k^2}{\Omega_k}, \quad (33)$$

while the second moment becomes

$$\begin{aligned} \mathcal{M}_k^{(2)} = \mathcal{M}_0^{(2)} + E_v \frac{\widetilde{F}_{kk} - \Omega_k^2}{\Omega_k} + \frac{\widetilde{F}_{kk} - \Omega_k^2}{2\Omega_k} \sum_{i \neq k} \frac{\widetilde{F}_{ii} - \Omega_i^2}{\Omega_i} + \frac{g_k^2}{\Omega_k} \\ + \frac{15}{8} \frac{(\widetilde{F}_{kk} - \Omega_k^2)^2}{\Omega_k^2} + \sum_{i \neq k} \frac{2\widetilde{F}_{ik}}{\Omega_i \Omega_k}. \end{aligned} \quad (34)$$

From the first and second moments, the standard deviation of the spectrum can be obtained:

$$\sigma = \left( \mathcal{M}^{(2)} - \left( \mathcal{M}^{(1)} \right)^2 \right)^{1/2}. \quad (35)$$

Furthermore, to get an *a priori* estimate of the suitability of a particular normal mode for VIPER excitation, we compute the ratio of the intensities of the transition from the pre-excited vibrational state  $|\mathbf{0}' + 1_k\rangle$  versus the ground vibrational state  $|\mathbf{0}'\rangle$  to the ground vibrational state of the excited electronic state  $|\mathbf{0}\rangle$ :

$$\frac{\langle \mathbf{0}' + 1_k | \mathbf{0} \rangle}{\langle \mathbf{0}' | \mathbf{0} \rangle} = \frac{S_k}{\sqrt{2}} \quad (36)$$

with the column vector  $\mathbf{S}$  given by

$$\mathbf{S} = 2\boldsymbol{\delta}' \left( \mathbf{1} - \boldsymbol{\Omega}'^{1/2} \mathbf{J} \mathbf{X}^{-1} \mathbf{J}^T \boldsymbol{\Omega}'^{1/2} \right), \quad (37)$$

with

$$\mathbf{X} = \mathbf{J}^T \boldsymbol{\Omega}' \mathbf{J} + \boldsymbol{\Omega}. \quad (38)$$

where  $\boldsymbol{\Omega}'$  and  $\boldsymbol{\Omega}$  are the diagonal matrices of the ground and excited state's vibrational frequencies, respectively, and  $\boldsymbol{\delta}' = \mathbf{K}^T \boldsymbol{\Omega}'^{1/2}$  is the vector of the dimensionless displacements along the ground state normal modes. These displacements are a useful quantity for determining the difference between the two states' equilibrium structures.

It is evident from Eq. (37) that the ratio of the vibronic transitions in question is mainly proportional to the dimensionless shift, i.e. the displacement between the equilibrium structures. The Duschinsky mixing and the vibrational modes' frequency change upon excitation also enters, though, in the second term, i.e., the matrix expression in Eq. (37).

## IV. Computational procedure

Three molecular systems were investigated in this work, two of which have already been studied experimentally.<sup>2,3</sup> The laser dye Coumarin 6 is the first system that was investigated experimentally using the VIPER approach.<sup>2</sup> The other two systems, i.e., [7-(diethylamino)coumarin-4-yl]methyl-azide (DEACM-N<sub>3</sub>) and *para*-Hydroxyphenacyl thiocyanate (*p*HP-SCN), are model systems for photo-cleavable caging groups,<sup>4</sup> with the azide and thiocyanate groups representing the leaving group, respectively.

Electronic structure calculations were performed with the *Gaussian09* package, revision *D.01*,<sup>21</sup> using density functional theory (DFT) for the ground state and its time-dependent extension (TD-DFT) for the excited state. Geometry optimizations and harmonic vibrational analyses in the ground state were performed using analytical first and

second derivatives, respectively. For the excited state, numerical differentiation of analytic gradients was used to obtain second derivatives. Tight optimization criteria in combination with fine integration grids (`int=ultrafine`) were used throughout. Solvent effects were treated using the polarizable continuum model (PCM). For Coumarin 6 and DEACM-N<sub>3</sub> the long-range-corrected hybrid functional  $\omega$ B97x-D<sup>22</sup> was used exclusively. Due to computational issues (see below), different density functionals were used for *p*HP-SCN, including the CAM-B3LYP<sup>23</sup> and PBE0<sup>24</sup> hybrid functionals. All electronic structure calculations were performed using the Def2-TZVP<sup>25</sup> triple-zeta basis set.

For the numerical wavepacket propagation, the multi-layer ML-MCTDH variant<sup>8</sup> of the Multi-Configuration Time-Dependent Hartree method<sup>11</sup> was employed, using the Heidelberg MCTDH package, version 8.5.5.<sup>27</sup> The multi-layer tree representing the wavefunction partitioning was constructed from the bottom up by successively combining pairs of modes, as detailed in Appendix B. The primitive basis was built in a harmonic-oscillator Discrete Variable Representation (DVR).

Calculations of vibrationally resolved absorption spectra using the TI formalism were performed with a development version of the *FCclasses* code.<sup>14</sup> The excited-state PES was constructed using the adiabatic Hessian (AH) approach,<sup>26</sup> expanding the PES around its state-specific minimum. The TI computations were performed with  $N_{\text{max}} = 10^8$ , and the resulting stick spectra were convoluted with a Lorentzian lineshape with a HWHM of 0.01 eV.

Complementary TD calculations were performed by the two methods described above, i.e., the analytical approach of Sec. II.B.1 (also implemented in the *FCclasses* development version) and the numerical wavepacket approach detailed in Sec. II.B.2. All approaches refer to the same PES in the AH formulation as employed in the TI calculations. For the numerical wavepacket approach, the PES was expressed in ground-state normal modes, see Eq. (29); for this purpose, an in-house code was used. Time correlation functions obtained by either the analytical or numerical TD approach were subsequently Fourier transformed<sup>28</sup> to yield the absorption spectrum. Before Fourier transforming, the correlation functions  $\chi^0(t)$  were multiplied by a damping term,

$$\chi(t) = \chi^0(t) \cos\left(\frac{\pi}{2t_{\text{max}}}t\right) e^{-|t|/\tau} \quad (39)$$

where  $t_{\text{max}}$  is the time up to which the correlation function is calculated and  $\tau$  is the damping time. To match the spectral broadening applied to the spectra from the TI approach, a value of  $\tau = 65.8$  fs was chosen, corresponding to a Lorentzian HWHM of 0.01 eV.

## V. Results

Vibrational normal modes suitable for pre-excitation within the VIPER scheme should fulfill several criteria: they should have a strong infrared absorption cross section to achieve the largest possible signal strength and they should be well separated to allow for selective excitation using an infrared pulse with an FWHM of approximately 8 to 20  $\text{cm}^{-1}$ . For the systems investigated here, experiments have been carried out in the range between 1500  $\text{cm}^{-1}$  and 1900  $\text{cm}^{-1}$ , which turns out to contain several promising modes in terms of VIPER activity. For all three systems, the lowest singlet excited state with significant oscillator strength was chosen for further investigation. In the following, we discuss theoretical results in relation to selected experimental Fourier-Transform Infrared (FTIR) and VIPER results.

### A. Coumarin 6

Coumarin 6 contains 43 atoms resulting in 123 vibrational normal modes. The most interesting modes in the context outlined above are the carbonyl stretch mode and two ring distortion modes in the coumarin moiety. Coumarin 6 shows a bright HOMO-LUMO transition with  $\pi$ - $\pi^*$  character on the coumarin moiety, exhibiting large oscillator strength.

Figure 3 shows the computed absorption spectrum of Coumarin 6 at zero temperature in THF, obtained with the methods outlined above. A good agreement between the different methods can be observed. The TD approach using the analytical autocorrelation function gives a slightly higher intensity in the high-frequency part of the spectrum than the TI approach. This effect can be attributed to the limited convergence of the TI approach because the integral calculation needs to be truncated, therefore neglecting a large number of very small integrals that are contributing to the high frequency part of the spectrum. For Coumarin 6, 94 % of the total spectral intensity are recovered with the chosen number of computed FC integrals. The analytical first moment of the spectrum is 25 156  $\text{cm}^{-1}$  whereas the resulting TI spectrum has a first moment of 24 985  $\text{cm}^{-1}$ .

The spectrum obtained by wavepacket propagation features a somewhat higher total intensity compared to the other methods and is also slightly blue-shifted with a first moment of 25 392  $\text{cm}^{-1}$ . In Fig. 3, this shift has been corrected by 90  $\text{cm}^{-1}$  to show the close agreement of the spectral shape and the detailed features. A slight discrepancy remains, due to the different intensity distributions.

The influence of vibrational pre-excitation on the electronic absorption spectrum of Coumarin 6 is shown in Fig. 4, together with experimental VIPER measurements. In the wavenumber range above 1580  $\text{cm}^{-1}$  only three bands appear, corresponding to two ring modes (labeled *RM 1* and *RM 2* for the low and high frequency mode, respectively) and one carbonyl stretch mode (labeled *CO*). In general, vibrational pre-excitation from the global

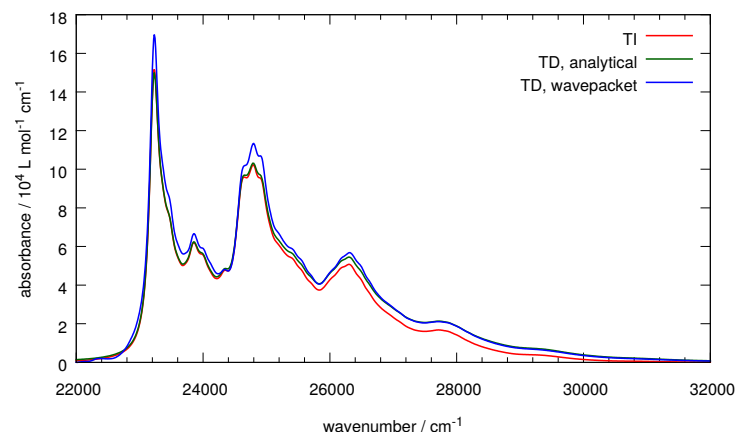


Figure 3: Computed absorption spectrum of Coumarin 6 in THF obtained from  $\omega$ B97x-D/Def2-TZVP calculations. Spectra were computed using the TI approach (red), Fourier transformation of the analytical autocorrelation function (green) and of the wavepacket autocorrelation function (blue). The spectrum obtained from the wavepacket propagation has been red-shifted by  $90\text{ cm}^{-1}$  (see text for discussion).

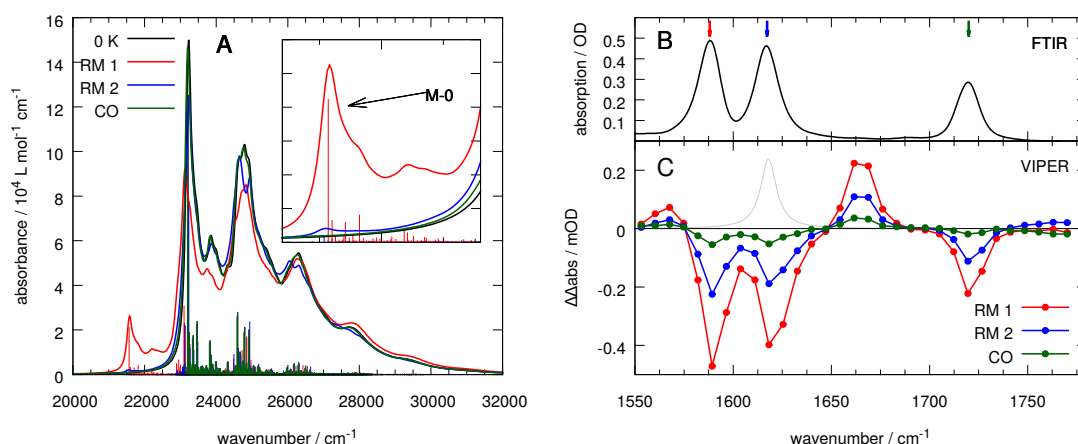


Figure 4: **(A)** Computed absorption spectra of Coumarin 6 in THF using the analytical autocorrelation function approach with  $\omega$ B97x-D/Def2-TZVP data. Spectra are shown without vibrational pre-excitation (black), with pre-excitation of the lower-frequency ring mode (red), the higher-frequency ring mode (blue) and the CO stretch mode (green). **(B)** Experimental FTIR absorption spectrum of Coumarin 6 in THF. **(C)** VIPER spectra of Coumarin 6 in THF after pre-excitation of the lower-frequency ring mode (red), the higher-frequency ring mode (blue) and the CO stretch mode (green). Experimental spectra were recorded using a concentration of 10 mM and a layer thickness of  $250\text{ }\mu\text{m}$ .

ground state induces additional vibronic transitions upon electronic excitation which have a lower energy than the 0-0-transition. In particular, transitions to the vibrational ground

state of the excited electronic state (denoted the M-0-transition) become feasible. These additional transitions induce a red-shift of the low-energy edge of the absorption band. An efficient VIPER excitation requires a high transition probability in this frequency range. In panel (A) of Fig. 4 the M-0 transition after excitation of the lower-frequency ring mode (red) is clearly visible, while the corresponding transitions resulting from excitation of the higher-frequency ring mode and the carbonyl stretch mode are much weaker. This finding is in agreement with the experimental results in panel (C) of Fig. 4, showing the largest VIPER signal upon excitation of the lower-frequency ring mode.

Interestingly, the first moment of the spectrum changes only very slightly upon pre-excitation; in case of the low-frequency ring mode it changes from  $25\,156\text{ cm}^{-1}$  to  $25\,082\text{ cm}^{-1}$ . On the other hand, the standard deviation of the spectrum increases from  $1744\text{ cm}^{-1}$  to  $2056\text{ cm}^{-1}$ , i. e. the spectrum gets broader while remaining constant in energy. The additional low-frequency transitions are countered by a more pronounced tail in the high frequency range (cf. panel (A) of Fig. 4).

For completeness, we also computed spectra at finite temperature, as documented in Appendix C. These show that the spectral structures are essentially unchanged, indicating that the VIPER excitation will give very similar results at non-zero temperature.

## B. 7-(Diethylamino)coumarin azide

In DEACM-N<sub>3</sub> the  $S_0$ - $S_1$  transition features a pronounced  $\pi$ - $\pi^*$ -character and is localized to the coumarin moiety, very similar to Coumarin 6. Due to the structural similarity, vibrational analysis of DEACM-N<sub>3</sub> yields again two distinct ring distortion modes and an intense CO stretch mode in the relevant IR frequency range.

The computed electronic absorption spectrum of DEACM-N<sub>3</sub> is shown in Fig. 5. The patterns present in the spectra of Coumarin 6 are also observed in this case. The analytical TD method again recovers most of the high-frequency part of the spectrum, while the convergence of the TI method is at 88 %. The first spectral moment has an analytical value of  $29\,964\text{ cm}^{-1}$  while the TI method gives a first moment of  $29\,642\text{ cm}^{-1}$ . The spectrum resulting from the wavepacket propagation is again blueshifted with a first moment of  $30\,204\text{ cm}^{-1}$  and also with a slightly higher intensity. However, the agreement of the features of the spectral lineshape is again very good.

Figure 6 shows the computed absorption spectra of DEACM-N<sub>3</sub> under the influence of vibrational pre-excitation, together with experimental VIPER measurements. Computations show strong additional redshifted transitions upon excitation of the lower frequency ring mode. In this case the first moment is slightly reduced to  $29\,918\text{ cm}^{-1}$  while the standard deviation increases from  $2013\text{ cm}^{-1}$  to  $2488\text{ cm}^{-1}$ . The other modes appear to have a much weaker effect on the spectrum. This observation is consistent with the corresponding

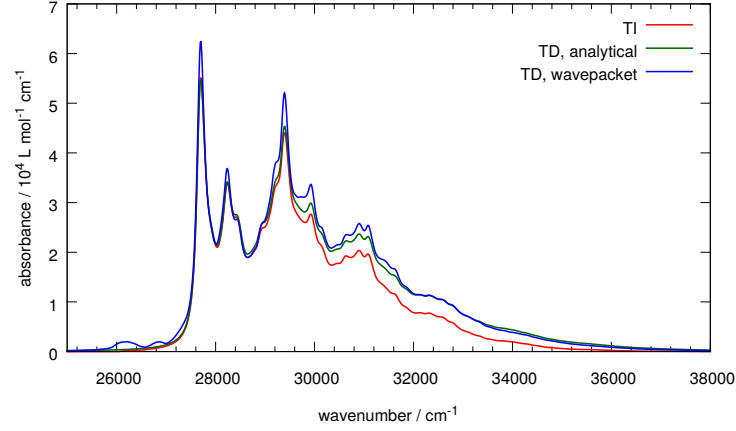


Figure 5: Computed absorption spectrum of DEACM-N<sub>3</sub> in acetonitrile obtained from  $\omega$ B97x-D/Def2-TZVP calculations. The color coding is equivalent to Fig. 3. The spectrum obtained from wavepacket propagation has been redshifted by 150 cm<sup>-1</sup>.

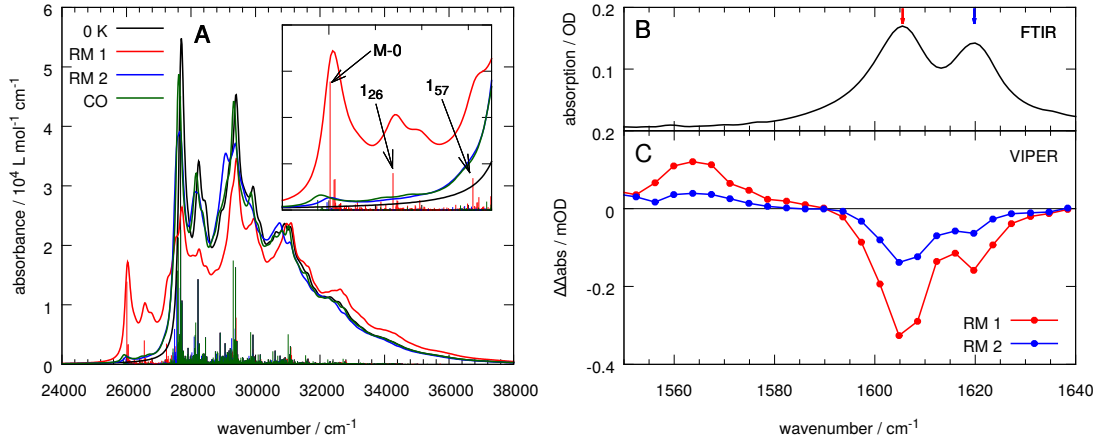


Figure 6: **(A)** Computed absorption spectra of DEACM-N<sub>3</sub> in acetonitrile using the analytical autocorrelation function approach with  $\omega$ B97x-D/Def2-TZVP data. Spectra are shown without vibrational pre-excitation (black), with pre-excitation of the lower-frequency ring mode (red), the higher-frequency ring mode (blue) and the CO stretch mode (green). **(B)** Experimental FTIR absorption spectrum of DEACM-N<sub>3</sub> in acetonitrile. **(C)** VIPER spectra of DEACM-N<sub>3</sub> in acetonitrile after pre-excitation of the lower-frequency ring mode (red) and the higher-frequency ring mode (blue). Experimental spectra were recorded using a concentration of 25 mM and a layer thickness of 250  $\mu$ m.



results from the calculations on Coumarin 6. This result again supports the experimental findings where the measured VIPER signal has a significantly higher intensity upon pre-excitation of the lower-frequency ring mode compared to the higher-frequency ring mode (see panel (C) of Fig. 6).

### C. *para*-Hydroxyphenacyl thiocyanate

Vibrational analysis of *p*HP-SCN yields two normal modes in the relevant frequency range, a ring distortion mode and a carbonyl stretch mode. However, these modes are not completely separable. The stretching of the carbonyl bond is accompanied by a slight distortion of the ring and vice versa for the ring distortion mode. The relative phase of these motions is combined with positive and negative sign, respectively, in the sense that the positive displacement along the ring distortion coordinate is accompanied by a shortening of the C=O bond in the case of the ring distortion mode and an elongation of the C=O bond in the case of the CO stretch mode.

The lowest singlet excited state of *p*HP-SCN with non-vanishing oscillator strength corresponds to a  $\pi$ - $\pi^*$ -transition in the benzene and carbonyl moiety. The excited-state structure of *p*HP-SCN posed a significant problem during the search for an excited state minimum. Depending on the choice of density functional and solvation model, significant state mixing, including exchange of oscillator strength between the state of interest and another, energetically close state, was observed, along with strong distortions of the molecular structure, including dissociation of the leaving group. This is an indication of nonadiabatic coupling between the involved states, necessitating a treatment with higher-level electronic structure methods such as CASSCF. In the following, results obtained with the  $\omega$ B97x-D density functional in THF are presented.

Figure 7 shows the computed spectra of *p*HP-SCN. Since there are no experimental VIPER measurements on *p*HP-SCN yet, this presents an opportunity to make theoretical predictions. In panel (A) the 0 K spectra obtained with the different methods show nearly quantitative agreement. The analytical first moment of the spectrum is  $37\,582\text{ cm}^{-1}$ , the TI and wavepacket method yield a value of  $37\,508\text{ cm}^{-1}$  and  $37\,726\text{ cm}^{-1}$ , respectively. The TI method is able to recover 98 % of the total intensity.

As shown in panel (B) of Fig. 7 vibrational pre-excitation of the ring distortion mode again has the strongest influence on the shape of the spectrum, shifting the analytical first moment to  $37\,601\text{ cm}^{-1}$  while increasing the standard deviation from  $1787\text{ cm}^{-1}$  to  $2428\text{ cm}^{-1}$ . However, contrary to the previous examples, the change of the spectrum induced by excitation of the CO stretch mode is non-negligible. In this case, the first moment is  $37\,367\text{ cm}^{-1}$  and the standard deviation is increased to  $2080\text{ cm}^{-1}$ .

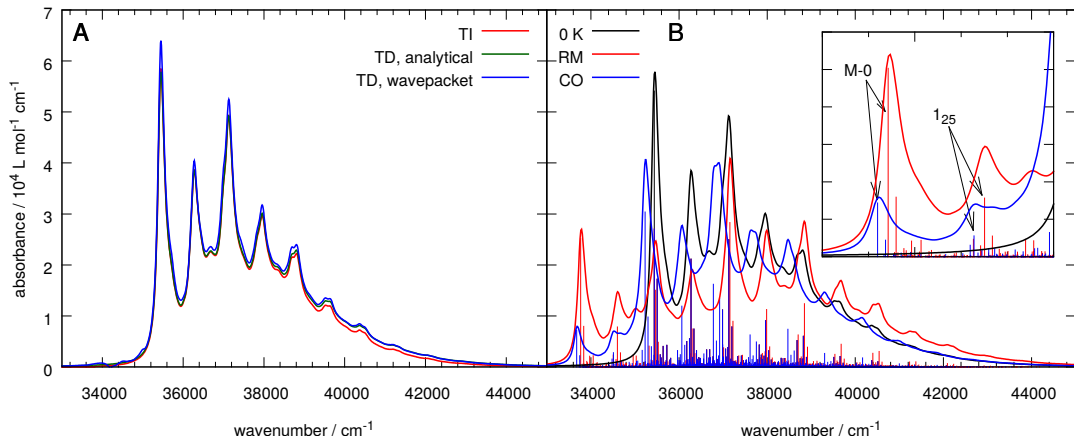


Figure 7: **(A)** Computed absorption spectra for *p*HP-SCN in THF obtained from  $\omega$ B97x-D/Def2-TZVP calculations. The color coding is equivalent to Fig. 3. The spectrum obtained from wavepacket propagation has been redshifted by  $45\text{ cm}^{-1}$ . **(B)** Absorption spectra computed with the analytical autocorrelation function method without vibrational pre-excitation (black), with excitation of the ring distortion mode (red) and the CO stretch mode (blue).

## VI. Discussion

The above results for electronic absorption spectra under the influence of vibrational pre-excitation illustrate good agreement between the different computational approaches, and show a pronounced mode-selectivity that is consistent with experiment. Excitation of ring distortion modes induces substantially stronger effects on the spectrum’s low-energy edge than localized stretching modes (e.g. carbonyl). These effects can be rationalized by analyzing the ratio of the M-0 to 0-0 transitions (cf. Eq. (37)). For the calculations detailed in Section V, the dimensionless displacements  $\delta$  and the intensity ratios  $S$  are given in Table 1.

Overall the correspondence between the values for  $S_k$  and the observed spectral line-shapes is very good. In the case of Coumarin 6, the lower-frequency ring mode has by far the highest intensity, while the intensity of the higher-frequency ring mode is much lower, and the CO stretch mode exhibits negligible intensity (cf. Fig. 4). In the case of DEACM-N<sub>3</sub>, the higher-frequency ring mode and the CO stretch mode have comparatively higher intensities which is also reflected in the computed spectra (cf. Fig. 6). In this case the CO stretch mode actually yields a slightly higher intensity than the higher-frequency ring mode. In *p*HP-SCN the difference between the intensity ratios is not as large as in the Coumarin-based systems. Here the CO stretch mode appears to be a reasonable choice as a candidate for VIPER excitation. In both Coumarin-based systems the theoretical predictions agree quite well with the experimental findings regarding the VIPER-efficiency

of the investigated normal modes.<sup>2,3</sup>

From Eq. (37) it is apparent that  $\delta'_k$  has a strong influence on  $S_k$ . In Table 1 the values for  $S$  are very similar to the corresponding  $\delta'$ -values. Additionally, in most cases  $S_k$  is lower in magnitude than  $\delta'_k$ , the only exception being the CO stretch mode of DEACM-N<sub>3</sub>. It appears that the displacement of a mode has a much greater influence on its suitability for VIPER excitation than the frequency change and the Duschinsky rotation which are both contributing to the matrix term in Eq. (37).

To further illustrate these points, Figure 8 schematically depicts the vibrational wavefunctions  $|\mathbf{0}' + 1_k\rangle$  and  $|\mathbf{0}\rangle$  whose overlap is critical to the VIPER effect for a simplified model system. Panel (A) shows the simplest case where the modes of the two electronic states coincide. By symmetry the overlap integral  $\langle \mathbf{0}' + 1_k | \mathbf{0} \rangle$  must vanish, even if the frequencies of the excited state modes differ from those of the ground state modes. Therefore, no VIPER transition can occur. Panel (B) shows a corresponding system where the ground state modes are simply rotated with respect to the excited state modes without any displacement. Again, by symmetry the integral vanishes. This can be shown formally by rewriting Eq. (37) using  $\mathbf{J} = \mathbf{1}$

$$S_k = 2\delta'_k \left( 1 - \frac{\Omega'_k}{\Omega'_k + \Omega_k} \right) \quad (40)$$

showing that if  $\delta'_k$  vanishes, so does  $S_k$ . Panel (C) shows a 1D cut of the system of panel (A) along  $q_l$ . Clearly, if no displacement is present, the overlap integral vanishes. In panel (D) a finite displacement between the PESs of the two electronic states is present, leading to a nonzero overlap between the vibrational states, as expressed by Eq. (37).

Table 1: Dimensionless displacements along the ground state normal modes  $\delta'_k$  and resulting transition intensity ratios  $S_k$  for the relevant normal modes of the systems investigated here. Data for Coumarin 6 and *p*HP-SCN is obtained from  $\omega$ B97x-D/Def2-TZVP calculations in THF while data for DEACM-N<sub>3</sub> results from  $\omega$ B97x-D/Def2-TZVP calculations in acetonitrile.

mode	Coumarin 6		DEACM-N <sub>3</sub>		<i>p</i> HP-SCN	
	$\delta'_k$	$S_k$	$\delta'_k$	$S_k$	$\delta'_k$	$S_k$
ring mode 1	0.612	0.603	-0.805	-0.809	-0.999	-0.988
ring mode 2	-0.179	-0.131	-0.237	-0.195	—	—
CO stretch	-0.053	-0.043	0.214	0.222	-0.554	-0.528

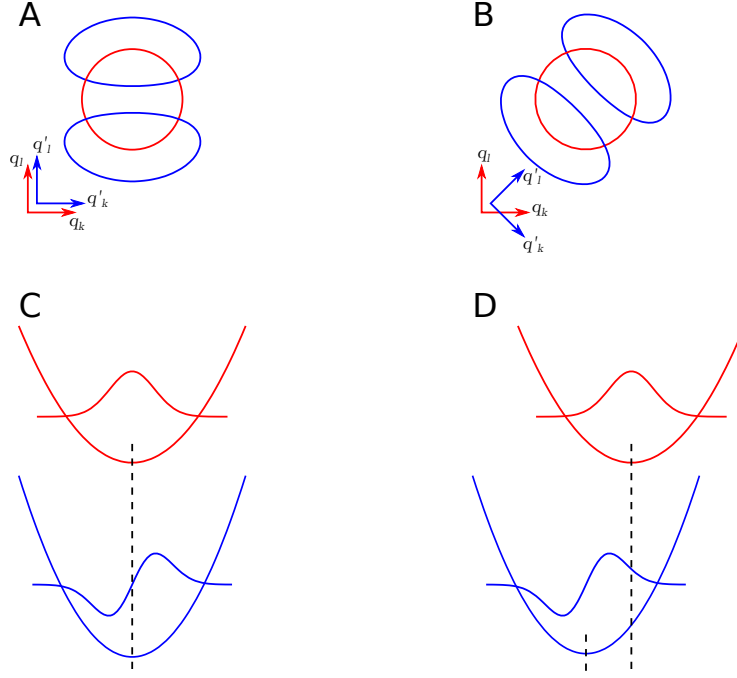


Figure 8: Schematic illustration of the influence of normal coordinates displacement vs Duschinsky rotation on the overlap of the pre-excited vibrational state  $|\mathbf{0}' + 1_k\rangle$  with the vibrational ground state  $|\mathbf{0}\rangle$ . **(A)** Contour view of the product wavefunction of modes  $q'_k$  and  $q'_l$ , where  $q'_l$  has been pre-excited (blue) and the corresponding wavefunction of  $q_k$  and  $q_l$  (red) which represents the vibrational ground state. **(B)** The same but with the ground state modes  $q'_k$  and  $q'_l$  rotated w. r. t. their excited state counterparts. Obviously, the overlap is equal in cases **(A)** and **(B)**. **(C)** Ground and excited state PES of a pre-excited mode along with the corresponding wavefunctions. The minima of both potentials are coinciding. **(D)** The same but with a finite displacement between the PESs. Obviously, the overlap is significantly different in cases **(C)** and **(D)**.

Finally, one should mention that the agreement between the different computational methods is good, but not perfect. Importantly, the spectral features match very well. However, the spectra obtained by wavepacket propagation are consistently blue-shifted relative to their respective analytical counterparts. This effect is likely to result from numerical inaccuracies in energetic offsets, or possibly from the limited convergence of the quantum dynamical propagation due to the finite basis size. In addition, the spectra obtained by wavepacket propagation tend to exhibit spurious structures below the 0-0 transition, which we also attribute to insufficient numerical convergence.

## VII. Conclusion and outlook

In this work we have presented complementary time-independent and time-dependent approaches for the computation of vibrationally resolved electronic absorption spectra including the effect of pre-excitation of a specific vibrational normal mode. Within the harmonic approximation to the potential energy surfaces, the three methods that were employed – the time-independent *FCclasses* approach and the time-dependent analytical and numerical wavepacket approaches – formally coincide, and in practice yield good numerical agreement. At this level of treatment, analytical approaches are indeed attractive and efficient alternatives to the more general numerical wavepacket approach (see also Refs. [29,30] for related analytical developments).

In the present context, these methods were applied to three chromophores to investigate their suitability for excitation with the VIPER mixed IR/VIS pulse sequence. We have shown that vibrational pre-excitation leads to an intense M-0 vibronic transition if the equilibrium structure of the excited state features a large displacement along the selected mode with respect to the ground state equilibrium configuration. In this context the role of Duschinsky mixing appears to be less important; in particular a purely rotated vibrational structure without any displacement is shown not to yield any M-0 transitions. The effect of pre-excitation is most pronounced if the electronic transition involves the same structural region of the molecule as the pre-excited normal mode, resulting in a strong vibronic coupling.

Follow-up work will tend to favor the time-dependent approach, in view of including effects of Intramolecular Vibrational Redistribution (IVR) and simulating the full VIPER experiment. While the evaluation of FC integrals and of the analytical autocorrelation function require harmonic PESs, high-dimensional wavepacket propagation is a flexible strategy and can be performed on coupled surfaces line in the case of Linear (LVC) or Quadratic (QVC) Vibronic Coupling models,<sup>31</sup> and on anharmonic surfaces as well. This opens the road for investigations of both excitations to states exhibiting strong nonadiabatic couplings and the vibrationally hot system’s dynamics on the anharmonic ground

state potential energy surface during the time between the IR and the VIS pulse. Experimental observations<sup>2</sup> suggest a decay of the vibrational excitation within about 5 ps.

## **Acknowledgement**

We thank Robert Binder for preliminary work on the Coumarin 6 system. We gratefully acknowledge funding by the Deutsche Forschungsgemeinschaft via RTG 1986 “Complex Scenarios of Light Control”.

## References

- <sup>1</sup>L. van Wilderen and J. Bredenbeck, *Angew. Chem. Int. Ed.* **54**, 11624 (2015).
- <sup>2</sup>L. van Wilderen, A. T. Messmer, and J. Bredenbeck, *Angew. Chem. Int. Ed.* **53**, 2667 (2014).
- <sup>3</sup>D. Kern-Michler et al., in preparation.
- <sup>4</sup>P. Klán et al., *Chem. Rev.* **113**, 119 (2012).
- <sup>5</sup>F. Santoro, R. Improta, A. Lami, J. Bloino, and V. Barone, *J. Chem. Phys.* **126**, 084509 (2007).
- <sup>6</sup>F. Santoro, A. Lami, R. Improta, and V. Barone, *J. Chem. Phys.* **126**, 184102 (2007).
- <sup>7</sup>F. Santoro, A. Lami, R. Improta, J. Bloino, and V. Barone, *J. Chem. Phys.* **128**, 224311 (2008).
- <sup>8</sup>H. Wang and M. Thoss, *J. Chem. Phys.* **119**, 1289 (2003).
- <sup>9</sup>O. Vendrell and H. Meyer, *J. Chem. Phys.* **134**, 044135 (2011).
- <sup>10</sup>H.-D. Meyer, U. Manthe, and L. S. Cederbaum, **165**, 73 (1990).
- <sup>11</sup>M. H. Beck, A. Jäckle, G. A. Worth, and H.-D. Meyer, *Phys. Rep.* **324**, 1 (2000).
- <sup>12</sup>G. A. Worth, H. Meyer, H. Köppel, L. S. Cederbaum, and I. Burghardt, *Int. Revs. Phys. Chem.* **27**, 569 (2008).
- <sup>13</sup>F. Duschinsky, *Acta Physicochimica U.R.S.S.* **7**, 551 (1937).
- <sup>14</sup>F. Santoro, FCclasses, a Fortran 77 code, <http://village.pi.iccom.cnr.it/software>.
- <sup>15</sup>F. Santoro and A. Lami, Time-dependent approaches to calculation of steady-state vibronic spectra: From fully quantum to classical approaches, in *Computational Strategies for Spectroscopy: From Small Molecules to Nano Systems*, edited by V. Barone, chapter 10, pages 475–516, John Wiley & Sons, Inc., 2012.
- <sup>16</sup>F. Avila Ferrer, J. Cerezo, J. Soto, R. Improta, and F. Santoro, *Comp. Theor. Chem.* **1040–1041**, 328 (2014).
- <sup>17</sup>D. Tannor, *Introduction to quantum mechanics: A time-dependent perspective*, University Science Books, USA, 1st edition, 2007.
- <sup>18</sup>A. Baiardi, J. Bloino, and V. Barone, *J. Chem. Theory Comput.* **9**, 4097 (2013).

- <sup>19</sup>Q. Peng, Y. Niu, C. Deng, and Z. Shuai, Chem. Phys. **370**, 215 (2010).
- <sup>20</sup>M. Biczysko, J. Bloino, F. Santoro, and V. Barone, Time-independent approaches to simulate electronic spectra lineshapes: From small molecules to macrosystems, in *Computational Strategies for Spectroscopy: From Small Molecules to Nano Systems*, edited by V. Barone, chapter 8, pages 361–443, John Wiley & Sons, Inc., 2012.
- <sup>21</sup>M. J. Frisch et al., Gaussian 09 Revision D.01, Gaussian Inc. Wallingford CT.
- <sup>22</sup>J.-D. Chai and M. Head-Gordon, Phys. Chem. Chem. Phys. **10**, 6615 (2008).
- <sup>23</sup>T. Yanai, D. P. Tew, and N. C. Handy, Chem. Phys. Lett. **393**, 51 (2004).
- <sup>24</sup>C. Adamo and V. Barone, J. Chem. Phys. **110**, 6158 (1999).
- <sup>25</sup>F. Weigend and R. Ahlrichs, Phys. Chem. Chem. Phys. **7**, 3297 (2005).
- <sup>26</sup>F. J. A. Ferrer and F. Santoro, Phys. Chem. Chem. Phys. **14**, 13549 (2012).
- <sup>27</sup>G. A. Worth, M. H. Beck, A. Jäckle, O. Vendrell, and H.-D. Meyer, The MCTDH Package, Version 8.5.4 See <http://mctdh.uni-hd.de/>.
- <sup>28</sup>W. H. Press, S. A. Teukolsky, W. T. Vetterling, and B. P. Flannery, *Numerical Recipes 3rd Edition: The Art of Scientific Computing*, Cambridge University Press, New York, NY, USA, 3rd edition, 2007.
- <sup>29</sup>J. Huh and R. Berger, Faraday Discuss. **150**, 363 (2011).
- <sup>30</sup>J. Huh and R. Berger, J. Phys.: Conf. Ser. **380**, 012019 (2012).
- <sup>31</sup>H. Köppel, W. Domcke, and L. S. Cederbaum, in *Conical Intersections*, edited by W. Domcke, D. R. Yarkony, and H. Köppel, pages 323–368, World Scientific Co., 2004.



## Appendix A. Derivation of the analytical autocorrelation function

Starting from Eq. (16) of Sec. II.B.1, we now introduce an orthogonal transformation to sum and difference coordinates,  $\mathbf{Z} = (\mathbf{Q}_e + \bar{\mathbf{Q}}_e)/\sqrt{2}$ ,  $\mathbf{U} = (\mathbf{Q}_e - \bar{\mathbf{Q}}_e)/\sqrt{2}$ , to simplify the integrals, in line with Ref. [18]. This results in

$$\begin{aligned} \chi_k(t) = & 2\mu_0^2 \Gamma_{gk} e^{i(E_0/\hbar + \omega_{gk})t} \sqrt{\frac{\det(\mathbf{\Gamma}_g) \det(\mathbf{a}_e)}{\pi^N (2\pi i \hbar)^N}} \exp[-\mathbf{K}^T \mathbf{\Gamma}_g \mathbf{K}] \int d\mathbf{Z} \int d\mathbf{U} \\ & \times \left( K_k^2 + \sqrt{2} K_k \sum_l J_{kl} Z_l + \frac{1}{2} \sum_l \sum_m J_{kl} J_{km} (Z_l + U_l)(Z_m - U_m) \right) \\ & \exp\left[-\frac{1}{2} \mathbf{Z}^T \mathbf{D} \mathbf{Z} - \sqrt{2} \boldsymbol{\lambda}^T \mathbf{Z}\right] \exp\left[-\frac{1}{2} \mathbf{U}^T \mathbf{C} \mathbf{U}\right] \quad (\text{A1}) \end{aligned}$$

where we used  $\boldsymbol{\lambda}^T := \mathbf{K}^T \mathbf{\Gamma}_g \mathbf{J}$  in addition to the definitions of Eq. (21).

The terms that are linear in  $U_l$  and  $U_m$  give no contribution to the integral and can therefore be eliminated. Additionally, the notation can be simplified by defining the vector  $\boldsymbol{\alpha}^{(k)}$  with  $\alpha_l^{(k)} = J_{kl}$  and the matrix  $\boldsymbol{\beta}^{(k)}$  with  $\beta_{lm}^{(k)} = J_{kl} J_{km}$ :

$$\begin{aligned} \chi_k(t) = & 2\mu_0^2 \Gamma_{gk} e^{i(E_0/\hbar + \omega_{gk})t} \sqrt{\frac{\det(\mathbf{\Gamma}_g) \det(\mathbf{a}_f)}{\pi^N (2\pi i \hbar)^N}} \exp[-\mathbf{K}^T \mathbf{\Gamma}_g \mathbf{K}] \int d\mathbf{Z} \int d\mathbf{U} \\ & \left( K_k^2 + \sqrt{2} K_k (\boldsymbol{\alpha}^{(k)})^T \mathbf{Z} + \frac{1}{2} \mathbf{Z}^T \boldsymbol{\beta}^{(k)} \mathbf{Z} - \frac{1}{2} \mathbf{U}^T \boldsymbol{\beta}^{(k)} \mathbf{U} \right) \\ & \exp\left[-\frac{1}{2} \mathbf{Z}^T \mathbf{D} \mathbf{Z} - \sqrt{2} \boldsymbol{\lambda}^T \mathbf{Z}\right] \exp\left[-\frac{1}{2} \mathbf{U}^T \mathbf{C} \mathbf{U}\right] \quad (\text{A2}) \end{aligned}$$

Before proceeding, we simplify the prefactor by using

$$e^{i\frac{E_0}{\hbar}t} = \prod_k e^{i\frac{\hbar}{2}\Gamma_{gk}t} = \det\left(e^{i\frac{\hbar}{2}\mathbf{\Gamma}_g t}\right) = \sqrt{\frac{1}{\det(e^{-i\hbar\mathbf{\Gamma}_g t})}} \quad \text{and} \quad \mathbf{a}'_g(t) = \frac{2i\hbar\mathbf{\Gamma}_g}{e^{-i\hbar\mathbf{\Gamma}_g t}} \quad (\text{A3})$$

and split the autocorrelation function into three components:

$$\chi_k(t) = 2\Gamma_{gk} e^{i\hbar\Gamma_{gk}t} \left[ K_k^2 \chi_{FC}^0(t) + K_k \chi_{k,a}^0(t) + \chi_{k,b}^0(t) \right] \quad (\text{A4})$$

with

$$\begin{aligned} \chi_{FC}^0(t) = & \mu_0^2 \sqrt{\frac{\det(\mathbf{a}'_g(t) \mathbf{a}_e(t))}{(2\pi i \hbar)^{2N}}} \exp[-\mathbf{K}^T \mathbf{\Gamma}_g \mathbf{K}] \int d\mathbf{Z} \int d\mathbf{U} \\ & \exp\left[-\frac{1}{2} \mathbf{Z}^T \mathbf{D} \mathbf{Z} - \sqrt{2} \boldsymbol{\lambda}^T \mathbf{Z}\right] \exp\left[-\frac{1}{2} \mathbf{U}^T \mathbf{C} \mathbf{U}\right] \quad (\text{A5}) \end{aligned}$$

$$\chi_{k,a}^0(t) = \sqrt{2}\mu_0^2 \sqrt{\frac{\det(\mathbf{a}'_g(t)\mathbf{a}_e(t))}{(2\pi i\hbar)^{2N}}} \exp\left[-\mathbf{K}^T \mathbf{\Gamma}_g \mathbf{K}\right] \int d\mathbf{Z} \int d\mathbf{U} \left(\boldsymbol{\alpha}^{(k)}\right)^T \mathbf{Z} \exp\left[-\frac{1}{2}\mathbf{Z}^T \mathbf{D} \mathbf{Z} - \sqrt{2}\boldsymbol{\lambda}^T \mathbf{Z}\right] \exp\left[-\frac{1}{2}\mathbf{U}^T \mathbf{C} \mathbf{U}\right] \quad (\text{A6})$$

$$\chi_{k,b}^0(t) = \frac{1}{2}\mu_0^2 \sqrt{\frac{\det(\mathbf{a}'_g(t)\mathbf{a}_e(t))}{(2\pi i\hbar)^{2N}}} \exp\left[-\mathbf{K}^T \mathbf{\Gamma}_g \mathbf{K}\right] \int d\mathbf{Z} \int d\mathbf{U} \left(\mathbf{Z}^T \boldsymbol{\beta}^{(k)} \mathbf{Z} - \mathbf{U}^T \boldsymbol{\beta}^{(k)} \mathbf{U}\right) \exp\left[-\frac{1}{2}\mathbf{Z}^T \mathbf{D} \mathbf{Z} - \sqrt{2}\boldsymbol{\lambda}^T \mathbf{Z}\right] \exp\left[-\frac{1}{2}\mathbf{U}^T \mathbf{C} \mathbf{U}\right] \quad (\text{A7})$$

where  $\chi_{FC}^0(t)$  is the FC correlation function at 0 K while  $\chi_{k,a}^0(t)$  and  $\chi_{k,b}^0(t)$  are analogous to mixed Franck-Condon/Herzberg-Teller and Herzberg-Teller terms, respectively.<sup>18</sup> The integrals in Eq. (A5) can be solved by using the substitutions  $\mathbf{Z}_1 = \mathbf{D}^{1/2} \mathbf{Z} + \sqrt{2}\mathbf{D}^{1/2} \boldsymbol{\lambda}$  and  $\mathbf{U}_1 = \mathbf{C}^{1/2} \mathbf{U}$ , resulting in

$$\chi_{FC}^0(t) = \mu_0^2 \sqrt{\frac{\det(\mathbf{a}'_g(t)\mathbf{a}_e(t))}{(2\pi i\hbar)^{2N} \det(\mathbf{C} \mathbf{D})}} \exp\left[-\mathbf{K}^T \mathbf{\Gamma}_g \mathbf{K}\right] \exp\left[\boldsymbol{\lambda}^T \mathbf{D}^{-1} \boldsymbol{\lambda}\right] \int d\mathbf{Z}_1 \exp\left[-\frac{1}{2}\mathbf{Z}_1^T \mathbf{Z}_1\right] \int d\mathbf{U}_1 \exp\left[-\frac{1}{2}\mathbf{U}_1^T \mathbf{U}_1\right] \quad (\text{A8})$$

where the Gaussian integrals are known:

$$\int d\mathbf{Z}_1 \exp\left[-\frac{1}{2}\mathbf{Z}_1^T \mathbf{Z}_1\right] = \int d\mathbf{U}_1 \exp\left[-\frac{1}{2}\mathbf{U}_1^T \mathbf{U}_1\right] = (2\pi)^{N/2} \quad (\text{A9})$$

So we finally arrive at

$$\chi_{FC}^0(t) = \mu_0^2 \sqrt{\frac{\det(\mathbf{a}'_g(t)\mathbf{a}_e(t))}{(i\hbar)^{2N} \det(\mathbf{C} \mathbf{D})}} \exp\left[-\mathbf{K}^T \mathbf{\Gamma}_g \mathbf{K} + \boldsymbol{\lambda}^T \mathbf{D}^{-1} \boldsymbol{\lambda}\right]. \quad (\text{A10})$$

The same technique can be applied to the integrals in Eqs. (A6) and (A7) to obtain

$$\chi_{k,a}^0(t) = -2\chi_{FC}^0(t) \left(\boldsymbol{\alpha}^{(k)}\right)^T \mathbf{D}^{-1} \boldsymbol{\lambda} \quad (\text{A11})$$

and

$$\chi_{k,b}^0(t) = \frac{1}{2}\chi_{FC}^0(t) \left(2\boldsymbol{\lambda}^T \mathbf{D}^{-1} \boldsymbol{\beta}^{(k)} \mathbf{D}^{-1} \boldsymbol{\lambda} + \text{Tr}[\boldsymbol{\beta}^{(k)}(\mathbf{D}^{-1} - \mathbf{C}^{-1})]\right) \quad (\text{A12})$$

The above expression is equivalent to Eq. (18) of the main text, when taking into account the additional definitions specified in Sec. II.B.1.

## Appendix B. Construction of the ML-MCTDH tree

Within the ML-MCTDH framework, the wavefunction is defined in terms of a tree structure consisting of combinations of single-particle functions. In Fig. 9, the structure of the multi-layer tree is illustrated. The tree was constructed by first ordering the normal modes with increasing frequency. The lowest-layer particles were built by combining adjacent pairs of normal modes into one particle, creating two-dimensional subspaces. If the total number of normal modes is odd, the last particle contains three modes instead of two. The lowest-level particles are then again combined pairwise, forming the particles of the next higher layer. This process is continued until only two or three particles remain, which then constitute the top layer.

## Appendix C. Spectra at finite temperature

The analytic formulation of the autocorrelation function as given in Sec. II.B.1 automatically includes temperature effects, providing spectra at finite temperatures with little extra computational cost. Our treatment of the VIPER excitation presented here assumes a 0 K initial state because the frequencies of the vibrational modes that are involved in the vibrational pre-excitation are much higher than  $kT$  at room temperature. Nonetheless, spectra at finite temperature were computed to check whether these spectra are simply broadened with respect to the zero-temperature case, or whether any additional vibronic transitions from excited vibrational states arise. Figure 10 shows computed absorption spectra of Coumarin 6 confirming that increasing the temperature simply leads to a broadening of the vibronic fine-structure and no additional lower-energy transitions are observed.

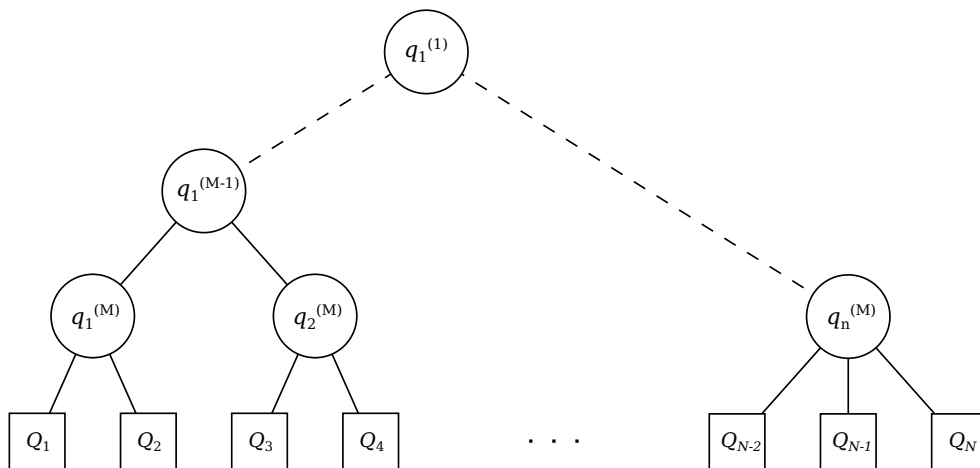


Figure 9: Schematic representation of the multilayer tree structure where  $N$  normal modes are arranged into  $M$  layers.

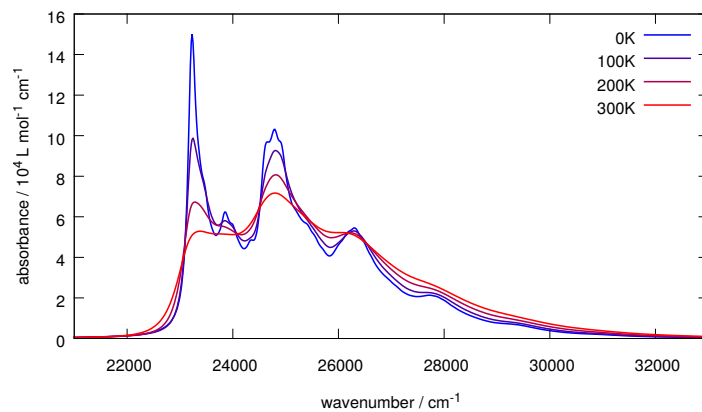


Figure 10: Computed spectra of Coumarin 6 in THF at different temperatures obtained from  $\omega$ B97x-D/Def2-TZVP calculations using the analytic autocorrelation function approach.